K.V. Mani, A. Cervone, F. Topputo
Combined Chemical–electric Propulsion for a Stand-Alone Mars Cubesat
Journal of Spacecraft and Rockets, In press-Published online 13/08/2019
doi:10.2514/1.A34519

Combined Chemical–Electric Propulsion for a Stand-Alone Mars CubeSat

Karthik V. Mani[a]
Politecnico di Milano, Via La Masa 34, 20156 Milan, Italy

Angelo Cervone[b]
Delft University of Technology, Kluyverweg 1, 2629HS Delft, the Netherlands

Francesco Topputo[c]
Politecnico di Milano, Via La Masa 34, 20156 Milan, Italy

Stand-alone interplanetary CubeSats require primary propulsion systems for orbit maneuvering and precise trajectory control. The current work focuses on the design and performance characterization of the combined chemical–electric propulsion systems that shall enable a stand-alone 16U CubeSat mission on a hybrid high-thrust–low-thrust trajectory from a Supersynchronous Geostationary Transfer Orbit to a circular orbit about Mars. The high-thrust chemical propulsion is used to escape Earth and to initiate stabilization at Mars. The low-thrust electric propulsion is used in heliocentric transfer, ballistic capture, and circularization. For chemical propulsion, design and performance characteristics of a monopropellant thruster and feed system utilizing ADN-based FLP-106 propellant are presented. For electric propulsion, a performance model of an Iodine-propelled inductively coupled miniature radiofrequency ion thruster is implemented to calculate the variation of thrust, specific impulse and efficiency with input power. A power constrained low-thrust trajectory optimization utilizing the thruster performance model is pursued to calculate the transfer time, ΔV and the required propellant mass for fuel-optimal and time-optimal transfers. Overall, the combined chemical–electric systems yield a feasible propulsion solution for stand-alone CubeSat missions to Mars that balances propellant mass and transfer time.

Nomenclature

A = Ion thruster cross sectional area [m^2]

A_c = Combustion chamber area [m^2]

A_{eff} = Effective area for ion and electron wall losses [m^2]

[a]PhD Researcher, Department of Aerospace Science and Technology, Politecnico di Milano, karthikvenkatesh.mani@polimi.it.
[b]Associate Professor, Department of Space Engineering, Delft University of Technology, a.cervone@tudelft.nl, AIAA Member
[c]Associate Professor, Department of Aerospace Science and Technology, Politecnico di Milano, francesco.topputo@polimi.it. AIAA Member.

A_{eff1} = Effective area for ion wall neutralization [m^2]

A_g = Grid area for neutral gas [m^2]

A_{surf} = Total surface area [m^2]

A_{sr} = Surface recombination area [m^2]

A_t = Nozzle throat area [m^2]

C_F = Coefficient of thrust

c^* = Characteristic velocity [m/s]

D_c = Chamber diameter [m]

D_t = Nozzle throat diameter [m]

E_g = Neutral gas energy [J/m^3]

E_e = Electron energy [J/m^3]

E = Plasma process potential [J]

e = Electron charge [C]

g_0 = Gravitational accelemration [m/s^2]

h_L, h_R = Edge-to-centre plasma density ratios

ΔH_f^0 = Heat of formation [kJ/mol]

I_{beam} = Beam current [A]

I_{sp} = Specific impulse [s]

K = Collision rate factor [m^3/s]

k = Specific heat ratio

κ = Thermal conductivity [W/mK]

L_c = Chamber length [m]

L_{con} = Nozzle constriction length [m]

$\mathfrak{M}$ = Molecular mass [amu]

m = Mass [kg]

$\dot{m}$ = Mass flow rate [kg/s]

n = Number density [$1/m^3$]

p = Plasma process power [W/m^3]

P = Power [W]

P_c = Combustion chamber pressure [Pa]

Q_0 = Particle flow rate [Pa]

q_{th} = Rate of thermal diffusion [W/m^3]

R = Radius [m]

R_{gas} = Gas constant [kJ/kmol − K]

r = Spacecraft distance [km]

$\mathcal{R}$ = Resistance [Ω]

T = Thrust [N]

$\mathcal{T}_c$ = Combustion temperature [K]

$\mathcal{T}_e$ = Electron temperature [K]

$\mathcal{T}_g$ = Neutral gas temperature [K]

t_s = Residence time [s]

u = Throttle factor

$u_{Bohm,i}$ = Ion bohm velocity [m/s]

V = Plasma chamber volume [m^3]

V_c = Combustion chamber volume [m^3]

v_g = Gas velocity [m/s]

$v_{beam,i}$ = Ion beam velocity [m/s]

w = Particle number density rate due to plasma processes [$1/m^3s$]

β = Grid transparency

Γ = Particle flux [$1/m^2s$]

ε = Expansion area ratio

η_c = Combustion efficiency

η_n = Nozzle efficiency

η_p = Thruster power efficiency

η_m = Mass utilization efficiency

η_{tot} = Total efficiency

κ_B = Boltmann constant [J/K]

Λ_0 = Heat diffusion length [m]

μ = Gravitational parameter of Earth [km^3/s^2]

Ω_{el} = Rate of electron-neutral elastic collisions [W/m^3]

Ω_{in} = Rate of ion-neutral elastic collisions [W/m^3]

I. Introduction

CubeSats have been in usage for Earth-based missions since the turn of the century for multifarious applications including Earth-observation, climate assessment, lower thermosphere characterization, and biological research [1]. Development of such CubeSats has primarily been pursued by Universities and small-spacecraft consortia. Contemporary CubeSats lack primary propulsion systems and are incapable of performing major orbital maneuvers. However, recent mission studies using micropropulsion options have indicated the feasibility of CubeSats to perform such maneuvers [2–4].

Owing to the significant increase in efforts to enhance CubeSat capabilities, multiple propulsion systems are currently being developed [5]. Chemical propulsion systems applicable to CubeSats include monopropellant, bipropellant, solid motors and cold gas thrusters [6]. Electric propulsion systems for CubeSat applications include gridded ion thrusters, Hall thrusters, field emission electric propulsion, pulsed plasma thrusters and helicon thrusters [7–9]. Other innovative solutions include dual mode thrusters that have a high-thrust chemical mode and a high-I_{sp} electric mode [10].

Interplanetary CubeSats development will be a necessary step for increasing the solar system exploration efforts at high science-to-investment ratio [11]. CubeSat Missions to Mars could be achieved through: a) in-situ deployment by a mothership and b) highly flexible stand-alone CubeSats on deep-space cruise. The MarCO mission, designed by JPL and launched alongside InSight lander mission in May 2018, is the only interplanetary CubeSat in existence [12]. The mission is injected directly into the interplanetary space by the launcher and performs a Mars flyby to provide communication support during InSight's landing. The CubeSats use Vacco MiPS (Micro CubeSat Propulsion System) for executing two trajectory control maneuvers. Stand-alone CubeSats to near-Earth objects are shown to be feasible, such as the Miniaturised Asteroid Remote Geophysical Observer (M-ARGO) mission study by the European Space Agency [13]. Improvements to communication, power, and propulsion systems could push the envelope to 1.5 AU, thereby making a stand-alone Mars CubeSat feasible. Mission applications include Mars science observation and Mars communication relay network setup [12, 14].

Stand-alone CubeSat missions from Earth to Mars require robust primary propulsion systems for precise trajectory control and orbital manoeuvring. On-board propulsion increases their launch flexibility and autonomy. The launch could be shared with any primary payload that is bound for a highly-elliptic orbit, for example Supersynchronous Geostationary Transfer Orbit (SSGTO), as the frequency of such launches is high. From there, the CubeSat shall escape Earth, pursue a deep-space cruise, and finally enter an orbit about Mars. The main motivation for this work is to provide propulsion solutions that enable such missions.

In this work, section II delineates the mission characteristics of Mars Atmospheric Radiation Imaging Orbiter (MARIO), a 30 kg 16U CubeSat mission to Mars, and the usage of combined propulsion in tandem with hybrid high-thrust–low-thrust trajectory. The CubeSat shall escape Earth within a short timeframe using high-thrust chemical propulsion and perform a deep-space cruise using low-thrust electric propulsion. Fully-chemical transfers are fast

but lead to an excessive system mass. Fully-electric transfers save mass but have untenable transfer times. Hybrid transfer solutions that utilize chemical–electric propulsion achieve a balance between system mass and transfer time. The spacecraft then experiences a ballistic capture and is emplaced on a circular orbit about Mars. The emphasis is on the word *combined*, since chemical and electric propulsion are *separate systems present in the same spacecraft*, and are operated alternatively.

The remainder of the paper is organized as follows: in section III, performance and design characteristics of a monopropellant thruster utilizing ADN-based FLP-106 green propellant are presented. High-thrust Earth-escape trajectory design and feed system sizing are expounded. In section IV, a performance model of an Iodine-propelled inductively coupled miniature radiofrequency gridded ion thruster is implemented to calculate the thrust, specific impulse, and efficiencies. Variation of performance with input power is obtained, which is crucial for the power constrained low-thrust trajectory optimization. An optimal control problem is solved to compute the low-thrust trajectory, overall ΔV, and the required propellant mass. In section V, some conclusions are drawn and details on further research are presented.

II. Mission overview

MARIO is a stand-alone CubeSat exploration mission to Mars that shall demonstrate the capabilities of CubeSats to perform a) orbit raising & Earth escape, b) low-thrust deep-space cruise c) ballistic capture at Mars and d) acquisition of the final operating orbit. These are the 4 key phases of this mission.

The injection orbit is a highly-eccentric SSGTO with a perigee of 295 km and an apogee of 90,000 km. Such injection orbits are commonplace for contemporary geostationary satellite missions that utilize electric propulsion for apogee reduction and circularization to GEO; e.g. Falcon 9 v1.1 rocket launched Thaicom 6 in January 2014 into this orbit and Thaicom 8 in May 2017 into a 350 km $\times$ 90226 km orbit[a]. Owing to the higher number of communication satellite launches ($>$ 5 per year) compared to deep-space launches ($\sim$1 per year), this orbit is selected to (a) improve the launch opportunities and widen the launch window, (b) reduce the ΔV required for Earth escape, and (c) provide more flexibility and autonomy to the CubeSat mission by diminishing its dependence on larger interplanetary spacecraft.

Swift escape is required to avoid excessive radiation damage since the spacecraft crosses the Van Allen radiation belts. A high-thrust chemical propulsion system is required to provide high ΔV within a short duration. A low-thrust electric propulsion system instead will drastically increase the residence time of the spacecraft in the radiation belts. The maneuvers are split and multiple orbit raisings are pursued to effectively distribute the ΔV and achieve Earth escape within a short timeframe while controlling gravity losses. Figure 1a illustrates the orbit raising and escape using chemical propulsion.

[a]Space Launch Report - Falcon 9
`http://www.spacelaunchreport.com/falcon9ft.html` and `https://www.spacex.com/missions`. Last visited: 10-Mar-2019

Once Earth escape is achieved, the deep-space cruise or heliocentric transfer to Mars is executed using low-thrust high-specific impulse electric propulsion (Figure 1b). Two strategies are investigated: a) time-optimal continuous thrusting and b) fuel-optimal bang-bang thrusting control. The critical resource for the electric propulsion system is the available power, and the specific impulse and thrust depend on it.

At the end of the cruise, the spacecraft experiences a *ballistic capture* (Figure 1c). This is a phenomenon through which the spacecraft is *captured* into a temporary stable orbit about Mars, only by the virtue of the natural attractions of Mars and the Sun [15]. The orbit acquired by the spacecraft after ballistic capture is highly irregular, and thus unusable for continuous observation missions. A high-thrust maneuver is performed to reduce the initial eccentricity and stabilize the orbit. The circularization to 60,000 km orbit is completed through low-thrust propulsion (Figure 1d). At this orbit, the planned thermal camera payload will characterise the temperature in the Mars upper atmosphere.

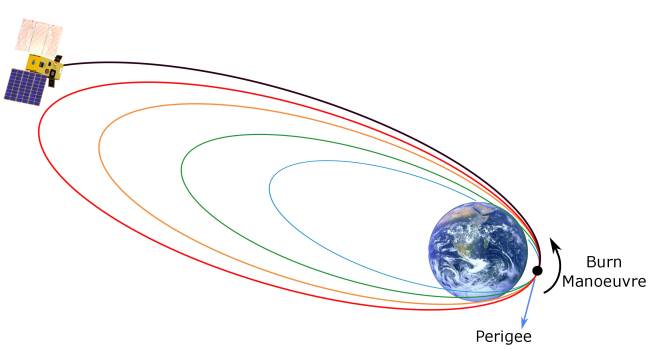

(a) Orbit raising and Earth escape.

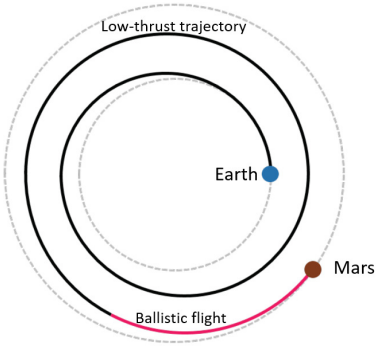

(b) Deep-space cruise and ballistic capture

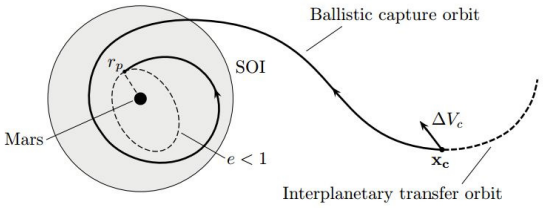

(c) Ballistic capture mechanism [15]

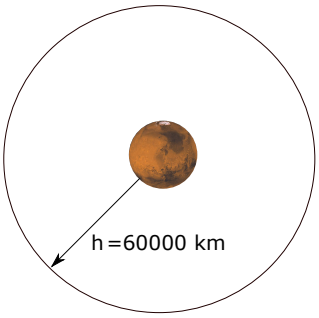

(d) Mars circular orbit

Fig. 1 MARIO Mission Phases

III. Chemical Propulsion

The primary requirements for the chemical propulsion system for the MARIO mission pertain to maximum thrust, ΔV, maximum burn duration, mass and safety. The propulsion system requirements are listed in Table 1.

The rationale for CP-01 comes from the ΔV required for Earth escape and initial stabilization at Mars. The initial insertion orbit parameters are $\{a, e, i, \Omega, \omega, \theta\}$ = {51526 km, 0.8705, 0.01°, 0°, 0°, 0°}. The velocity at perigee is

Table 1 Chemical Propulsion System Requirements

ID	Requirement
CP-01	The system shall provide a minimum ΔV = 445 m/s for orbital transfer and Mars orbit stabilization maneuvers.
CP-02	The system shall have a maximum thrust of 3 N
CP-03	The maximum thrusting time shall be 600 seconds per orbital maneuver
CP-04	The total mass of the chemical-electric propulsion systems shall be no more than 15 kg
CP-05	The system shall utilize non-toxic propellants

10.57 km/s and the corresponding escape velocity is 10.93 km/s. Thus, the ΔV for escape is is ~360 m/s, considering a theoretical impulsive maneuver. A 10% margin on ΔV is considered to include for gravity losses and other miscellaneous operational errors, thereby yielding a margined $\Delta V_{esc,mg}$ of 396 m/s. The deceleration maneuver for initial stabilization after ballistic capture requires a ΔV_{stab} of 45 m/s. An additional ~10% margin is placed and the $\Delta V_{stab,mg}$ is 49 m/s.

Performance requirement CP-02 establishes a limitation on thrust and CP-03 establishes the maximum burn time. For a 30 kg spacecraft, this combination effectively distributes the ΔV required to escape Earth into multiple maneuvers for transfer time reduction and gravity loss control. A single burn maneuver to escape leads to a gravity loss of ~23%, which is unacceptable in terms of operations and systems design (leads to a drastic increase of mass). A 1 mm thrust misalignment is considered, which is similar to LUMIO - a 12U lunar CubeSat mission [16]. The disturbance torque is 3 mNm with the maximum thrust. Reaction wheels sets with high maximum torque and momentum storage are utilized to compensate for the disturbance [17]. Thrust vectoring is also essential for controlling the momentum build-up. Additionally, maximum burntime limit is fixed to avoid excessive heat build-up in the thruster. The maximum mass requirement, CP-04, is constrained at 50% of the overall spacecraft mass for the combined chemical–electric propulsion system. Usage of green non-toxic propellants is required (CP-05) because the CubeSat is assumed to be a secondary payload and any damage to the primary spacecraft as well as any self-damage must be avoided. In addition to these, waivers on some of the traditional CubeSat requirements, like maximum pressure of 7 bar [7], are needed for executing the mission.

A. System types and trade-off

Selection of chemical propulsion system type is crucial as it has to be compatible with the MARIO mission. Trade-off of possible design options is conducted based on the thrust level, specific impulse, system mass, system complexity, control capabilities, reliability and technology readiness level. The systems under consideration are monopropellant, bipropellant, solid and cold gas thrusters. The thrust level must meet CP-02 and the minimum value should be high enough to expedite Earth escape. Specific impulse is a key design parameter, with higher values driving down system mass. Higher propellant densities are desired as the system size should be compatible with 16U form factor of the

CubeSat. Since CubeSat design has traditionally involved the use of commercial off-the-shelf equipment, the technology readiness level (TRL) of the system type is also important.

Figure 2 illustrates the propulsion trade-off. The choice of monopropellant systems for MARIO mission application is clear. Cold gas and solid thrusters are unacceptable in terms of thrust level, specific impulse, and system mass [6, 7]. Mono- and bipropellant system thrusts satisfy the requirement. Although, to reach the maximum thrust level, two such thrusters will be required. Monopropellant thrusters that use ammonium dinitramide (ADN) blends and bipropellant thrusters that use hydrogen peroxide (H_2O_2) and ethanol (C_2H_5OH) have sufficiently high specific impulses for the system mass to be compatible with the mission [18, 19]. They also satisfy the non-toxicity requirement CP-05.

Complexity plays a major role in system selection. Bipropellant feed system design and integration is extremely complicated for CubeSat applications and requires years of further development. The maturation of bipropellant systems for small satellite missions is very low and they are prone to valve failures and improper propellant mixing, thus posing an unacceptable risk to the mission. Monopropellant thrusters are relatively less complicated compared to them but they compromise on the performance [19]. Monopropellant systems using green propellants are also space qualified [20].

Criteria / Options	Thrust level	I_{sp}	Mass	Complexity	Control	Reliability	TRL
Cold gas	red Very low < 1 N	red Very low < 80 s	red Not compatible with required ΔV	green Simple system	orange Long duration burn difficult.	blue High	green 9
Solid	red Very high > 5 N	orange Moderate 200–250 s	red Not compatible with required ΔV	green Simple system	red No start-stop capability. Prone to misfires	red Bad for current application	green 9
Monopropellant	green OK 1–1.5 N	green High 230–270 s	green Compatible with required ΔV	orange Relatively complicated system	orange Pressure-feed control needs improvement.	green Good	green 7
Bipropellant	green High 1.5–1.9 N	blue Very high 300–330 s	green Compatible with required ΔV	red Extremely complicated system	red Feed system development requires huge effort.	red Prone to failures in feed system	orange 4

blue Exceeds requirements green Meets requirements orange Correctable deficiencies red Unacceptable

Fig. 2 Comparison of chemical propulsion systems

B. Propellant properties and analysis

The propellant considered is a liquid blend of ADN - ammonium dinatramide ($NH_4[N(NO_2)_2]$), called FLP-106 with a liquid phase density of 1357 kg/m^3 at 25°C [18]. In comparison, the widely used monopropellant Hydrazine has a density of 1.004 kg/m^3 at room temperature and has a very high toxicity. Hydrazine is classified within hazard 1 class explosive materials and has restrictions on transportation. FLP-106 does not fall into this category due to its very low sensitivity and volatility [21]. The I_{sp} yield of FLP-106 is also significantly higher than that of Hydrazine [22].

Thermochemical analysis of FLP-106 using the NASA Chemical Equilibrium Analysis (CEA) code is pursued to obtain the propellant performance [23]. ADN is a solid white salt with ammonia cation (NH_{4^+}) and dinitramide anion ($N(NO_2)_{2^-}$) which is readily soluble in water and other polar solvents [21]. FLP-106 consists of 64.6% ADN, 23.9 % water and 11.5% Monomethylformamide - MMF (C_2H_5NO) [22]. In the condensed phase, the heats of formation are: MMF ΔH_f^0 = -247.4 kJ/mol [24], ADN ΔH_f^0 = -134.6 kJ/mol [25], and Water ΔH_f^0 = -285.8 [26]. At P_c = 2 MPa and area ratio ε = 50 with frozen flow conditions at the exit, the analysis yields an ideal vacuum specific impulse $I_{sp,vac}$ = 258.2 s. Some key properties of FLP-106 and its performance are listed in Table 2.

Table 2 Properties of FLP-106 and performance prediction using NASA CEA at P_c = 20 bar and ε = 50 (frozen)

Property	Value	Property	Value
Molecular mass, $\mathfrak{M}$	22.8 kg/kmol	Characteristic velocity, c^*	1361.7 m/s
Liquid phase Density, ρ	1357 kg/m^3	Thrust coefficient, C_F	1.7985
Saturation temperature, T_s	273.15 K	Ideal specific impulse, I_{sp}	258.2 s
Vapour pressure, P_{vap}	<21 mPa	Combustion temperature, $\mathcal{T}_c$	2133.4 K

Two other comparable propellants are LMP-103S and AF-M315E, which are ADN and HAN - Hydroxylammonium Nitrate blends, respectively, and have a higher level of maturity [20, 27]. LMP-103S consists of 63% ADN, 13.95% water, 18.4% Methanol, and 4.65% Aqueous Ammonia (25%), which is similar to FLP-106 [22]. For the same thruster conditions, the specific impulse yield of LMP-103S using NASA CEA is 251.5 s. The density of LMP-103S is 1238 kg/m^3 [21]. The decrease in I_{sp} and density compared to FLP-106 shall lead to a larger propellant volume, which is a critical resource for a CubeSat. Although LMP-103S has been flight demonstrated, FLP-106 is preferred due ot its better performance and its presumed maturation within 2024 [28], at which the MARIO mission is envisaged to be launched.

AF-M315E has a higher density and similar I_{sp} compared to FLP-106. However, it has a higher health hazard [29]. Additionally, with AF-M315E being mildly acidic, long term storage is a major issue and it is compatible only with a limited set of materials. FLP-106 is much more safe to handle and can be stored for a longer period. Thus, for the current CubeSat mission application, FLP-106 is chosen.

C. Thruster performance and design

The thruster design is pursued with a target thrust of 3 N (CP-01). ADN-based thrusters providing 1 to 1.5 N thrust are currently under development [18, 20]. To provide the necessary thrust, two 1.5 N thrusters can be utilized.

The method of ignition and the ignition characteristics of the propellant play an important role in propulsion system design. Some studies utilize a hot catalytic bed for the decomposition of ADN [28]. The catalyst bed design is a complicated process and its analysis is out of the scope of this work. Wilhelm et al [30] have found that thermal ignition using a glowplug yields a stable flame and an acceptable ignition time for FLP-106 propellant. An exothermic reaction

that corresponds to ADN decomposition starts at 150°C [31]. The ignition temperature of FLP-106 is between 150°C to 200°C.

The chamber pressure is maintained at 2 MPa, which yields a similar thrust performance to the HPGP thruster on-board PRISMA satellite [20]. The CEA calculations yield ideal rocket performance parameters and the nozzle and combustion efficiencies need to be considered for real performance predictions.

A conical nozzle with a throat diameter, D_t, of 0.75 mm is utilized. From CEA calculations, the Reynold's number (Re) at the throat is $\sim$ 15000. The average nozzle efficiency η_n is 0.92 [32]. The combustion efficiency η_c is 0.95–0.99 for a well designed combustion chamber [32]. An average value of η_c = 0.98 is used. Application of these quality factors yields an I_{sp} of 232.8 s, which is considered low since it leads to a large propellant mass for the required ΔV.

The area ratio ε is increased and the variations of I_{sp} and T are studied to obtain the required performance and design parameters for the monopropellant thruster. A finite area combustion chamber with a nozzle contraction ratio of 50 is used and the constriction length L_{con} = 1.5 mm is chosen as a preliminary design value to achieve a 45° constriction angle. The mass flow rate $\dot{m}$ and subsequently the thrust are calculated using Eqs.1–3 [32].

$$\dot{m} = \frac{A_t \cdot P_c \cdot k}{\sqrt{(k \cdot R_{gas} \cdot \mathcal{T}_c)}} \cdot \sqrt{\left(\frac{2}{k+1}\right)^{(k+1)/(k-1)}} \tag{1}$$

$$T = \dot{m}\, c^*\, C_F \tag{2}$$

$$C_F = \eta_n\, C_{F,ideal} \quad \text{and} \quad c^* = \eta_c\, c^*_{ideal} \tag{3}$$

The thrust and the specific impulse increase with the increase in area ratio, as illustrated in Figure 3. The value of ε = 200 is chosen for the design. The rationale being that the corresponding performance values satisfy thruster requirements and higher ε values yield only a small increase in performance while leading to higher material usage and thruster mass. Additionally, very high ε values could lead to higher divergence losses, thereby reducing nozzle efficiency [32]. Thruster performance parameters for ε = 200 are listed in Table 3.

Table 3 Estimated thruster performance for ε = 200 using NASA CEA

Property	**Value**	**Property**	**Value**
Combustion efficiency, η_c	0.98	Characteristic velocity, c^*	1334.47 m/s
Nozzle efficiency, η_n	0.92	Thrust coefficient, C_F	1.7383
Max Thrust (per thruster)	1.536 N	Mass flow rate (per thruster), $\dot{m}$	0.673 g/s
Specific Impulse, I_{sp}	241.2 s	Exhaust velocity, v_e	2366.17 m/s
Chamber temperature, $\mathcal{T}_c$	2133.4 K		

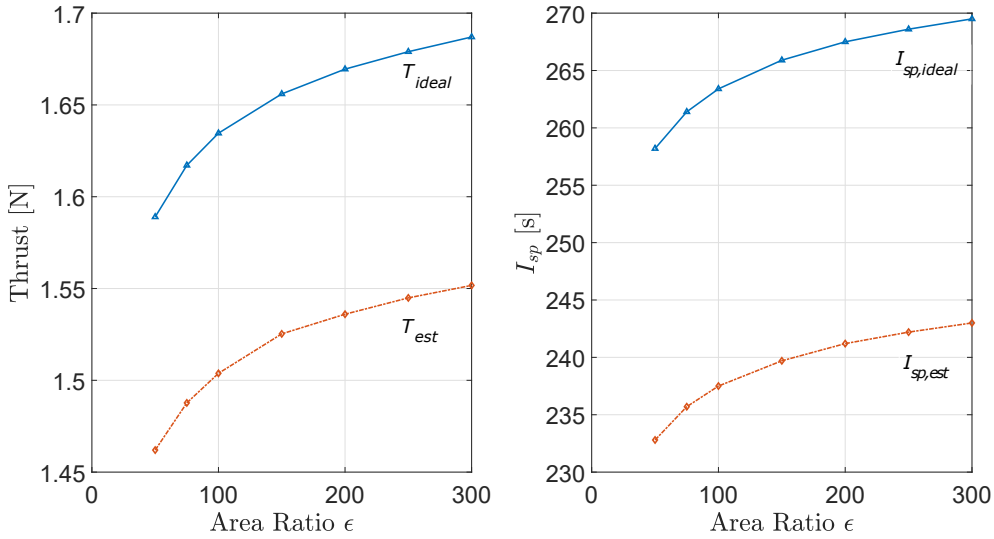

Fig. 3 Ideal and estimated T and I_{sp} variation with Area Ratio (ε). Total efficiency η_{tot} = 0.9016

For the combustion chamber design, the chamber volume V_c and chamber length L_c are calculated using Eqs. 4–5 [32].

$$V_c = t_s \; A_t \sqrt{k \; R_{gas} \; \mathcal{T}_c} \left(\frac{2}{k+1} \right)^{1/(k-1)} \tag{4}$$

$$L_c = \frac{V_c}{A_c} - L_{con} \left(1 + \sqrt{\frac{A_t}{A_c}} + \frac{A_t}{A_c} \right) \tag{5}$$

Here, the residence time t_s = 0.0026 s corresponds to the characteristic length L^* = 1.5 m, which in turn yields the maximum combustion performance [28, 30]. The chamber and nozzle design parameters are listed in Table 4. The thrusters are placed outside the 16U spacecraft structure.

Table 4 Monopropellant thruster design parameters

Parameter	**Value**	**Parameter**	**Value**
Thrusters	2	Throat diameter, D_t	0.75 mm
Chamber pressure, P_c	2 MPa	Contraction ratio, A_c/A_t	50
Chamber volume, V_c	662.7 mm^3	Expansion area ratio, ε	200
Chamber diameter, D_c	5.3 mm	Expansion half angle, α	15°
Chamber residence time, t_s	0.0026 s	Nozzle length (divergent), L_N	18.47 mm
Chamber length, L_c	28.26 mm	Thruster mass, $m_{thruster}$	0.2 kg [a]

[a] Value assumed based on state-of-the-art 1N monopropellant thrusters without valves Ariane Group - `http://www.space-propulsion.com/brochures/hydrazine-thrusters/hydrazine-thrusters.pdf` Last accessed: 04-April-2019

D. High-thrust trajectory analysis

Spacecraft trajectory is calculated by assuming a 2-body problem, discarding perturbations, and integrating the equations of motion with the calculated thruster performance and the injection orbit as input. The goal of the trajectory analysis is to find a) required burntime (t_b) for each maneuver, b) total number of maneuvers required to achieve Earth escape with the lowest flight time, c) the overall ΔV imparted to the spacecraft, and d) the overall propellant mass consumed.

Thrust is applied from $-t_b/2$ to $t_b/2$ about the perigee for the powered flight; while ballistic flight has none. Integration of equations of motion is performed until Earth escape ($e = 1$) is achieved.

$$\ddot{r} + \frac{\mu}{r^3}\boldsymbol{r} = \frac{\boldsymbol{T}}{m}; \quad \dot{m} = -\frac{|\boldsymbol{T}|}{I_{sp}\, g_0}; \quad \boldsymbol{T} = u\, T_{max}\, \frac{\boldsymbol{v}}{||\boldsymbol{v}||} \tag{6}$$

The total time until escape depends upon the thrust and burntime. A grid search is done to calculate the t_b for each maneuver based on the lowest overall flight time (powered and ballistic) until Earth escape. The sampled values of t_b for each maneuver range from 400 to 600 seconds.

The thruster performance values of $T = 3$ N (CP-01) and $I_{sp} = 241.2$ s are utilized in this analysis. The calculated t_b for each maneuver is 560.6 s and the total flight time $P = 792.55$ hours. This flight time is counted as the Earth orbiting time until eccentricity $e = 1$, and not the time to reach the Earth sphere of influence. The total number of maneuvers is 6 and the escape is achieved at the 7th orbit. The number of Van Allen belt crossings amount to 13. The orbital raising is illustrated in Figure 4.

The calculated cumulative ΔV_{esc} of the orbit raising and escape maneuvers is 362.72 m/s, which is ~3 m/s higher than the ideal ΔV for escape. This difference corresponds to the accumulated gravity losses (ΔV_{gl} ~1%). A 10% margin is placed on the ideal ΔV for contingency and $\Delta V_{esc,mg}$ is 396 m/s.

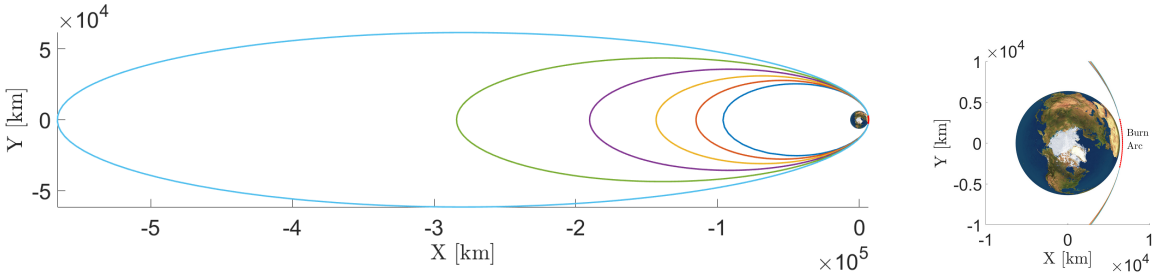

Fig. 4 MARIO orbit raising and escape - ballistic and burn trajectories

The propellant mass ($m_{p,mg}$) pertaining to $\Delta V_{esc,mg}$ is 4.623 kg while the m_p for ΔV_{esc} is 4.264 kg. The stabilization maneuver is executed after low-thrust heliocentric transfer and ballistic capture (section IV.E). The mission parameters and required thruster performance parameters are listed in Table 5

Table 5 Mission parameters for orbit raising and escape

Parameter	Value	Parameter	Value
Initial Mass, m_i	30 kg	Propellant mass (real), m_p	4.264 kg
Thrust, T	3 N	Propellant mass (margined), $m_{p,mg}$	4.623 kg
Specific Impulse, I_{sp}	241.2 s	Final mass at Earth escape, $m_{f,esc}$	25.736 kg [a]
Burn Time per maneuver, t_b	560.6 s	Mars stabilization ΔV_{stab}	45 m/s
Orbit raising maneuvers	6	Margined $\Delta V_{stab,mg}$ (∼10%)	49 m/s
Ideal ΔV	359.66 m/s	Propellant mass for ΔV_{stab}	0.393 kg
Real ΔV	362.72 m/s	Propellant mass for $\Delta V_{stab,mg}$	0.431 kg
Margined ΔV (10% margin)	396 m/s	Overall propellant mass, $m_{p,mg,ovr}$	5.054 kg

[a] Calculated based on the real m_p and not the margined.

E. System sizing and feed

The feed system consists of the storage tanks, valves, flow lines, and the tank pressurization system. The overall margined propellant mass (orbit raising + stabilization), $m_{p,mg} = 5.054$ kg for the monopropellant system with an $I_{sp} = 241.2$ s. Considering the liquid phase density of FLP-106 at room temperature (see Table 2), the propellant volume $V_p = 3724.4\,\text{cm}^3$, which in terms of CubeSat units is ∼ 3.7 U.

A regulated pressure-fed system is utilized as the thrust must be precise and constant [33]. Gaseous nitrogen GN_2 is used as the pressurant. A pressurized propellant tank requires a spherical or a cylindrical shape with elliptical dome ends to be safe. However, for a $3724.4\,\text{cm}^3$ tank, the radius of the spherical tank will be ∼9.62 cm, which leads to spatial accommodation issues in a 16U CubeSat. Thus, cylindrical tanks with elliptical dome ends are utilized. Assuming a ∼10% ullage volume, one large tank with 17 cm diameter would have a height of 19.4 cm. To save space and to accommodate rest of the feed system components, four tanks each with a capacity of 1025 cm^3 are utilized. Each tank has a radius of 4.7 cm and a height of 16.1 cm, occupying ∼1.6U space. These tanks are similar to the storage cell designs by Eagle Picher Technologies [34]. The tanks shape and the placement inside the spacecraft structure are illustrated in Figure 5.

The nominal feed pressure is set at 2.2 MPa and the Maximum Expected Operational Pressure (MEOP) is 2.6 MPa. The feed pressure value is similar to the one for a high-performance ADN-based monopropulsion system on-board PRISMA satellite [20]. A burst factor of 1.5 is applied on the MEOP to obtain the burst pressure. The pressurant gas (GN_2) pressure is considered to be 28 MPa at 323 K, at which the density is 257.8 kg/m^3 [35].

The material used for the tank is Titanium alloy Ti-6Al-4V. Its yield strength is 880 MPa and density is 4430 kg/m^3[36]. It has a very high corrosion resistance. The tank wall thickness is calculated for the burst pressure with a safety factor of 1.2 applied on the yield strength [37]. An additional safety factor of 2 is applied on the thickness considering launch loads and vibration. Precision machining techniques applied on Ti-6Al-4V enable the manufacturing

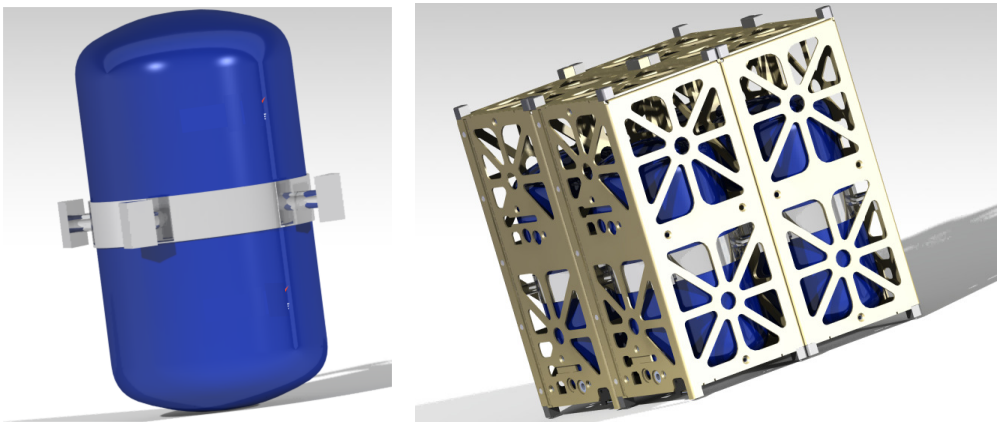

(a) Tank shape (b) 8U structure

Fig. 5 Tank shape and placement in the spacecraft structure

of tanks with small thicknesses [38]. The major components of the monopropellant thruster system are illustrated in Figure 6. The feed system design characteristics are listed in Table 6.

Table 6 Monopropellant system design parameters

Parameter	Value	Parameter	Value
Propellant tanks	4	Press. gas mass, m_{gas}	0.11 kg
Individual tank volume, V_{tank}	1025 cm^3	Press. tank volume, $V_{gas,tank}$	434.7 cm^3
Prop. feed pressure, P_{prop}	2.2 MPa	Press. tank radius, $r_{gas,tank}$	4.7 cm
Prop. tank burst pressure, $P_{prop,burst}$	3.9 MPa	Press. tank height, $h_{gas,tank}$	7.1 cm
Prop. tank radius, $r_{prop,tank}$	4.7 cm	Press. tank thickness, $th_{gas,tank}$	4.5 mm
Prop. tank height, $h_{prop,tank}$	16.1 cm	Press. tank mass, $m_{gas,tank}$	0.386 kg
Prop. tank thickness, $th_{prop,tank}$	0.50 mm	Feed pipes & valves mass, m_{fv}	0.20 kg
Total tank mass, m_{tank}	0.44 kg	Feed system total mass, m_{feed}	1.11 kg [a]
Press. gas pressure, P_{gas}	28 MPa	Feed system total volume	7.5U [b]
Overall propulsion system mass, $m_{cp,sys}$	6.59 kg		
Overall volume, $V_{cp,sys}$	7.5U		

[a] Feed system mass includes pressurant gas mass but not propellant mass
[b] Includes volumes of propellant tank, pressurant gas tank, valves, and pipes. Thrusters are placed outside the spacecraft structure.

IV. Electric Propulsion

Once Earth escape is achieved using the chemical propulsion system and the spacecraft reaches Earth's sphere of influence, the deep-space cruise phase starts. A high-I_{sp} electric propulsion system is utilized in this phase. The cruise lasts for ~3.5–4.5 years and culminates in ballistic capture [15]. Transfer to Mars after Earth escape could be achieved either by thrusting continuously, thereby minimizing flight time, or by thrusting intermittently to minimize propellant

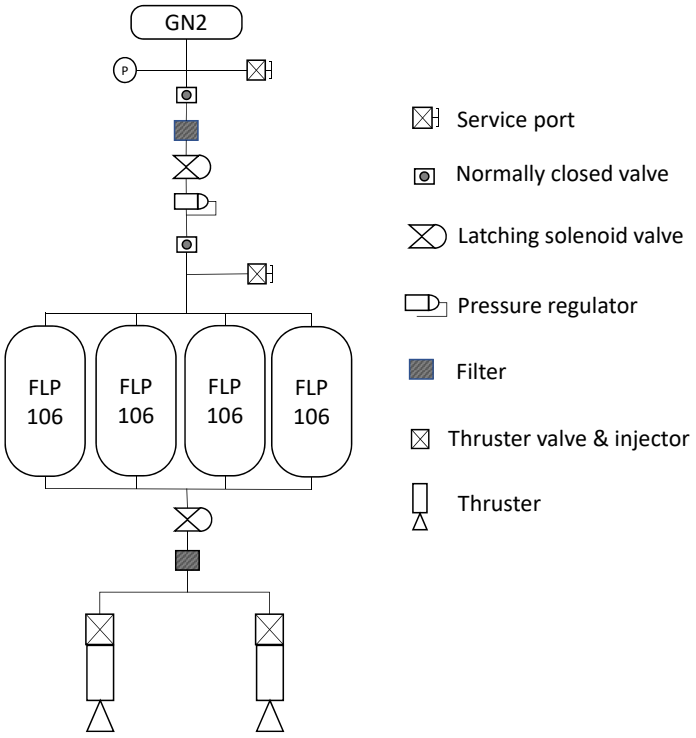

Fig. 6 Schematic of the monopropellant thruster system

consumption. Depending on the mission priority, one of the two techniques can be used. The requirements of the electric propulsion system and the heliocentric transfer are listed in Table 7.

Table 7 Electric propulsion requirements

ID	Requirement
EP-01	The maximum transfer time shall be 4.5 years for cruise and ballistic capture.
EP-02	The system shall have a maximum power consumption of 70 W
EP-03	The total mass of the chemical-electric propulsion systems shall be no more than 15 kg.

The rationale for EP-01 is to constrain the maximum transfer time such that valuable science products can be obtained before the end of the mission lifetime, ~6 years. Additionally, CubeSats have a lower endurance to deep-space conditions, thus limiting their lifetime. The science mission is scheduled for ~6 months and the circularization maneuvers to attain the orbit about Mars takes ~1.2 years (see Section IV.E).

Owing to the restricted power availability, EP-02 imposes a maximum limit on the power consumption of the thruster. Both thrust and I_{sp} vary with thruster power P_{th}. The power available to the electric propulsion system is calculated as a function of the distance between the spacecraft and the Sun. Figure 7 illustrates the available and consumed power for the MARIO mission. The total power generation at 1 AU is 175 W and at 1.5 AU is 74.3 W. Critical subsystems such as communications, on-board computer, attitude control, and electrical power system operate continuously during the

transfer. The combined power consumption of these subsystems is ~40 W. Cell degradation, neutralization losses and the power processing and control unit (PPCU) consumption (3 W) are included in the thruster input power calculations. The minimum power supplied to the thruster (at ~1.5 AU) is 30.4 W.

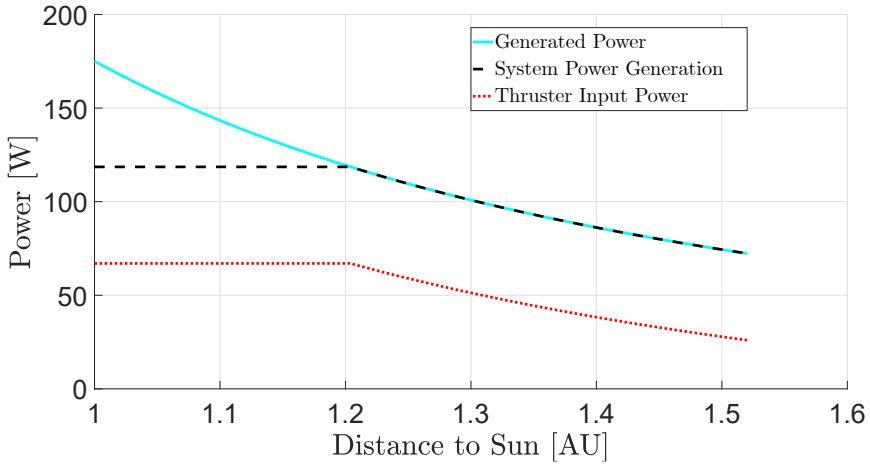

Fig. 7 Generated and consumed powers variation with the Sun-spacecraft distance for MARIO mission

A. System types

The choice of the electric propulsion system is very crucial as the thrusts, power consumptions, and the specific impulses vary significantly among system types. Applicability to CubeSat missions is crucial. The options are gridded ion, Hall, field emission electric propulsion, pulsed plasma, and helicon thrusters. A brief comparison is shown in Table 8.

Gridded ion thrusters applicable for small spacecraft have an I_{sp} in the range of 1500-3200 seconds and a propulsion lifetime in the order of 30,000 hours [39, 40]. Another suitable option would be the Hall effect thruster which has a lower I_{sp} but higher thrust for the same input power compared to a gridded ion thruster. Field emission electric propulsion (FEEP) thrusters have very high I_{sp} but also have a considerably high power consumption for the thrust produced [40]. Pulsed Plasma Thrusters (PPTs) have low I_{sp} and have a limit on propellant loading. Both, FEEP and PPT have low lifetimes [40]. While considering the heliocentric transfer time and the corresponding thruster operation time (EP-01), both FEEP and PPT are unsuitable for this mission application. Additionally, FEEP uses liquid metals such as cesium, indium and mercury as propellants, whose handling is extremely challenging and hazardous. Helicon thrusters are promising candidates but their low efficiency and lifetime pose a problem. Considering the lifetime, specific impulse and power consumption, the gridded ion thruster is chosen for the analysis and is well suited for MARIO mission application.

Table 8 Comparison of electric propulsion options

Type	Thrust [mN]	I_{sp} [s]	Power [W]	Life [hours]
Gridded Ion	0.5-1.6	1500-3200	30-80	~30000
Hall	1.8-4	800-1400	60-120	~10000
FEEP	0.35-2	>6000	28-160	<10000
Pulsed Plasma	0.01-1	500-1500	10-30	~1000
Helicon	0.8-1.5	900-1200	50-80	~1000

B. Propellant properties

Most common propellant for ion thruster applications is Xenon. It is a noble gas with a high molecular mass (131 amu) and a low ionization potential (12.13 eV). However, Xenon occurs only in trace amounts in the atmosphere and it is extracted as a byproduct in the oxygen separation process, thus making it very expensive (~$1140 per kg). A move towards an alternative propellant that has a similar molecular mass and ionization potential is necessary to reduce the costs while achieving similar performances to Xenon.

Iodine (I_2 or I), which is located adjacent to Xenon in the periodic table, is a good candidate and has a molecular mass 126.9 kg/kmol (monoatomic). It is a solid in standard atmospheric conditions with a density of 4940 kg/m^3. This eliminates the need for high pressure tanks, plumbing, and sophisticated thermal control systems, which are otherwise required in the case of Xenon. Iodine stored in a solid state in compact lightweight tanks can be moderately heated to sublimate and form I_2 vapour. This makes it highly suitable for deep-space CubeSat missions with high ΔV and subsequently large propellant mass requirements. The ionization potentials (E_{iz}) for I_2 and I are 9.3 eV and 10.45 eV, respectively, which are lower than that of Xenon. This contributes to a higher electrical efficiency. Additionally, the cost of pure Iodine is ~$400 per kg. Although Xenon ion thrusters have a great flight heritage, Iodine ion thrusters are well suited for the current mission application. Multiple Iodine ion thrusters have been developed, such as Busek BIT-3, which will be demonstrated in space on-board Lunar IceCube 6U CubeSat launched by NASA SLS Artemis-1 in 2020 [39].

One disadvantage of Iodine is its corrosive nature. However, using corrosion-resistant materials like MACOR or Alumina in plasma-generation chambers makes ion thruster compatible with Iodine. Thruster grids made out of Nickel–Chromium alloys like Hastelloy or Inconel have high resistance towards Iodine corrosion [41, 42]. Solar panels and other external surfaces do not suffer from Iodine corrosion due to the high vapour pressure of I_2, therefore its condensation is highly unlikely [43].

C. Thruster performance model

A performance model of an Iodine-fueled inductively coupled miniature radiofrequency gridded ion thruster is implemented following Grondein et al [44]. The performance parameters such as thrust, specific impulse, beam current and efficiencies are determined.

Solid Iodine is sublimated and I_2 vapour is injected into the chamber. Radiofrequency (RF) coils are placed around the thruster and a high frequency voltage is applied to the coils. Electromagnetic fields are used to heat the plasma electrons which in turn ionize the neutral gas [45]. There is no permanent applied magnetic field in RF ion thrusters. The ions produced are accelerated by a set of DC biased grids.

For the performance model, the chosen design and operational parameters are listed in Table 9. The thruster size is similar to that of the BIT-3 thruster [39]. A total mass flow rate of 48μg/s is chosen and the mass flow to the neutralizer cathode is fixed at 10%. The DC grid voltage V_{grid} is set at 2000 V.

Table 9 RF thruster performance model parameters

Parameter	Value	Parameter	Value
Thruster radius, R	1.25 cm	Grid transparency, β	0.6 (ion) & 0.3 (neutral)
Thruster length, L	2.2 cm	Mass flow rate, $\dot{m}_0$	48 μg/s
Chamber volume, V	10.792 cm^3	Particle flow rate, Q_0	1.14×10^{17} s^{-1}
RF coil radius, R_c	1.3 cm	Molecular mass, $\mathfrak{M}$	253.8 (I_2) & 126.9 (I)
No. of coils, N	5	Grid voltage, V_{grid}	2000 V
Grid separation, s	1 mm	Coil resistance, $\mathcal{R}_{coil}$	0.7 Ω

The neutral gas I_2 is injected with a flow rate of Q_0. Thrust is produced by the acceleration of I_2^+ and I^+ through the grids. Neutral gas thrust is produced by the fluxes of I_2 and I. A set of particle balance equations are written for all species in the model: e^-, I_2, I, I^-, I^+, I_2^+ to calculate their densities (n) as multiple processes take place in the plasma. The collision rate factors, K, are obtained from Grondein et al [44]. The particle number density rates due to plasma processes are: $w_{iz,I} = K_{iz,I}\, n_e\, n_I$ (I ionization), $w_{iz,I2} = K_{iz,I_2}\, n_e\, n_{I_2}$ (I_2 ionization), $w_{dissiz} = K_{dissiz}\, n_e\, n_{I_2}$ (I_2 dissociative ionization), $w_{diss} = K_{diss}\, n_e\, n_{I_2}$ (I_2 dissociation), $w_{dissatt} = K_{dissatt}\, n_e\, n_{I_2}$ (e^-–I_2 dissociative attachment), $w_{cex} = K_{cex}\, n_{I^-}\, n_{I_2^+}$ (I^-–I_2^+ charge exchange), $w_{ionrec} = K_{ionrec}\, n_{I^-}\, n_{I^+}$ (I^-–I^+ recombination). The atomic I surface recombination rate $w_{sr} = \frac{1}{8} n_I v_I \frac{\gamma_{sr}}{1-\gamma_{sr}} \frac{A_{sr}}{V}$. The surface recombination factor γ_{sr} is assumed be 0.02 [44]

$$\dot{n}_e = w_{iz,I} + w_{iz,I_2} + w_{dissiz} - w_{dissatt} - \frac{(\Gamma_{I^+} + \Gamma_{I_2^+})\, A_{eff}}{h_L\, V} \tag{7}$$

$$\dot{n}_{I_2} = \frac{Q_0}{V} - w_{dissiz} - w_{dissatt} - w_{iz,I_2} - w_{diss} + w_{cex} + w_{wr} + \frac{\Gamma_{I_2^+} A_{eff1}}{h_L\, V} - \frac{1}{4}\, n_{I_2}\, v_{I_2} \frac{A_g}{V} \tag{8}$$

$$\dot{n}_I = w_{dissiz} + w_{dissatt} - w_{iz,I} + 2\, w_{diss} + 2\, w_{ionrec} + w_{cex} - 2\, w_{sr} + \frac{\Gamma_{I^+} A_{eff1}}{h_L\, V} - \frac{1}{4}\, v_I\, n_I\, \frac{A_g}{V} \tag{9}$$

$$\dot{n}_{I^-} = w_{dissatt} - w_{ionrec} - w_{cex} \tag{10}$$

$$\dot{n}_{I^+} = w_{iz,I} + w_{dissiz} - w_{ionrec} - \frac{\Gamma_{I^+} A_{eff}}{h_L V} \tag{11}$$

$$\dot{n}_{I_2^+} = w_{iz,I_2} - w_{cex} - \frac{\Gamma_{I^+} A_{eff}}{h_L V} \tag{12}$$

$A_{eff} = 2\pi R^2 h_L + 2\pi R L h_R$ is the effective area for positive ion and electron wall losses, where h_L and h_R are edge-to-centre plasma denstiy ratios [46]. $A_{eff1} = \pi R^2 (2 - \beta_i) h_L + 2\pi R L h_R$ is the effective area for positive ion wall neutralization. $A_{sr} = \pi R^2 \left(2 - \beta_g\right) + 2\pi R L$ is the area for I surface recombination.

Electrons are produced by ionization of I_2 and I, and are lost by dissociative attachment with I_2 and their flux to the chamber walls. Atomic I is produced by the dissociation, dissociative ionization and dissociative attachment of I_2 as well as ion-recombination between I^+ and I^-. It is lost by the its ionization, wall recombination and ejection through the grids. Negative ions I^- are produced by dissociative attachment of I_2 and lost by ion-recombination and charge-exchange. Ionization of I and dissociative ionization of I_2 produce I^+ and they are lost by ion-recombination and ion flux through grids. Similarly, I_2^+ are produced by I_2 ionization and lost by charge exchange with I^- [44].

Neutral gas heating considers energy rates of elastic collisions of electrons–neutrals (Ω_{el}) and ions–neutrals (Ω_{in}) as well as thermal diffusion (q_{th}). The total gas energy $E_g = \frac{3}{2}(n_I + n_{I_2})\kappa_B \mathcal{T}_g$. The energy balance is given by Eq 13.

$$\dot{E}_g = \overbrace{3\frac{m_e}{\mathfrak{M}_I}\kappa_B(\mathcal{T}_e - \mathcal{T}_g)n_e n_I K_{el,I}}^{\Omega_{el,I}} + \overbrace{3\frac{m_e}{\mathfrak{M}_{I_2}}\kappa_B(\mathcal{T}_e - \mathcal{T}_g)n_e n_{I_2} K_{el,I_2}}^{\Omega_{el,I_2}} + \underbrace{\frac{1}{4}n_e\left(n_I \mathfrak{M}_I u^2_{Bohm,I^+} K_{in,I} + n_{I_2}\mathfrak{M}_{I_2} u^2_{Bohm,I_2^+} K_{in,I_2}\right)}_{\Omega_{in}} - \underbrace{\kappa\frac{\mathcal{T}_g - \mathcal{T}_{g0}}{\Lambda_0}\frac{A_{surf}}{V}}_{q_{th}} \tag{13}$$

where A_{surf} is the total surface area, κ is the thermal conductivity, κ_B is Boltmann constant, Λ_0 is the heat diffusion length, and $u_{Bohm,i}$ is the ion Bohm velocity [44].

Power (P_{RF}) supplied to the RF generator is partly absorbed by the plasma and partly dissipated at the coil. The absorbed power density $p_{abs} = \frac{1}{2}\mathcal{R}_{ind} I^2_{coil}/V$, where $\mathcal{R}_{ind}$ is the resistance of an equivalent circuit composed of plasma and the coil [46]. The coil power density $p_{coil} = \frac{1}{2}\mathcal{R}_{coil} I^2_{coil}/V$. The resistances are obtained using a transformer model based on Chabert et al [46]. Electron power is lost due to the plasma processes (e.g. ionization), electron–neutral elastic collisions, and ion losses at walls and grids [44]. The electron power balance is given by Eq. 14.

$$\dot{E}_e = p_{abs} - p_{iz,I} - p_{iz,I_2} - p_{dissiz} - p_{dissatt} - p_{diss} - p_{exc,I} - \Omega_{el,I} - \Omega_{el,I_2} - p_{wall} - p_{grid} \tag{14}$$

$$\text{with,} \quad p_{wall} = 7\kappa_B \mathcal{T}_e \left(u_{Bohm,I^+} n_{I^+} + u_{Bohm,I_2^+} n_{I_2^+} \right) \frac{A_{eff} - \pi R^2 h_L}{V}$$
$$p_{grid} = 6\kappa_B \mathcal{T}_e \left(u_{Bohm,I^+} n_{I^+} + u_{Bohm,I_2^+} n_{I_2^+} \right) \frac{A(1-\beta_i)}{V}$$

The power $p_{iz,I} = E_{iz,I}\, w_{iz,I}$, where $E_{iz,I}$ is the ionization potential of I. Similarly, the rest of the terms are calculated using their respective plasma process potentials such as E_{iz,I_2}, E_{dissiz}, $E_{dissatt}$, E_{diss}, and $E_{exc,I}$ (all expressed in Joules). Equations 7–14 are integrated to obtain plasma properties from which the performance values are calculated. The thrust, I_{sp}, and beam current I_{beam} are calculated using fluxes (Γ), ion beam velocities ($v_{beam,i} = \sqrt{2\, e\, V_{grid}/\mathfrak{M}}$), effective grid area of ions ($A\,\beta_i$) and neutrals ($A\,\beta_g$), and the mass flow rate ($\dot{m}_0$).

$$T = \Gamma_i\, \mathfrak{M}\, v_{beam,i}\, A\, \beta_i + \Gamma_g\, \mathfrak{M}\, v_{gas}\, A\, \beta_g \tag{15}$$
$$I_{sp} = \frac{T}{\dot{m}_0\, g_0} \qquad I_{beam} = e\, \Gamma_i\, A\, \beta_i \tag{16}$$

The ion and neutral fluxes, $\Gamma_i = h_L\, u_{Bohm,i}\, n_i$ and $\Gamma_g = \frac{1}{4}\, v_g\, n_g$, are calculated using positive ion and neutral densities (n), ion Bohm velocities ($u_{Bohm,i} = \sqrt{\mathcal{T}_e\, e/\mathfrak{M}}$), edge-to-centre plasma density ratio (h_L), and neutral gas velocities ($v_g = \sqrt{8\, \kappa_B\, \mathcal{T}_g/\pi\, \mathfrak{M}}$) [46]. The fluxes are calculated for ions I_2^+ and I^+, and neutrals gases I_2 and I. The molecular mass $\mathfrak{M}$ is 253.8 amu for I_2 and 126.9 amu for I.

Thruster power efficiency (η_p) is calculated using ion beam power ($P_{beam,i} = I_{beam,i}\, V_{grid}$), neutral thrust power ($P_g = \frac{1}{2}\, \mathfrak{M}\, v_g^2\, \Gamma_g\, A\, \beta_g$) and neutralizer cathode power (P_{cath}). The mass utilization efficiency (η_m) is the ratio of ejected ion flow rate ($\Gamma_i\, A\, \beta_i$) and injected gas flow rate (Q_0). Total efficiency is the product of η_p and η_m.

$$\eta_p = \frac{P_{beam,i} + P_g}{P_{beam,i} + P_g + P_{cath} + P_{RF}} \qquad \eta_m = \frac{\Gamma_i\, A\, \beta_i}{Q_0} \qquad \eta_{tot} = \eta_p\, \eta_m \tag{17}$$

The input RF power, P_{RF}, supplied to the coils is adjusted according to the available thruster power, P_{th} (see Figure 7). Fluxes Γ_i and Γ_g, and subsequently the powers $P_{beam,i}$ and P_g, depend upon P_{RF}. A simplified neutralizer cathode model based on Richardson's Law of thermionic emission is implemented to calculate the power, P_{cath}, required for ion beam neutralization [45]. The emitter is assumed to be composed of a tungsten filament coated with barium oxide. The emitter temperature is set at 1300 K and the efficiency is assumed to be 0.3. The total power P_{th} is the sum of $P_{beam,i}$, P_g, P_{cath} and P_{RF}.

The variations of thrust, I_{sp} and η with power are illustrated in Figure 8. As the input power increases, the power absorbed by the plasma increases. This results in an increase in ion flux and consequently the thrust. The required

neutralization power is 0.63–0.5% of the total power. The mass utilization efficiency increases and the thruster power efficiency decreases with the increase in power. The thruster performance values are listed in Table 10.

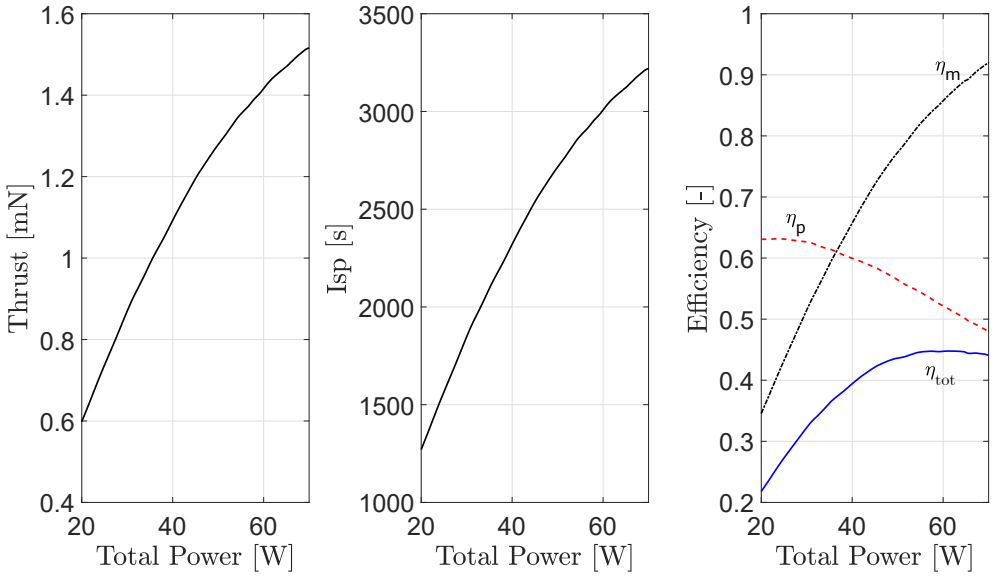

Fig. 8 Thrust, I_{sp} and efficiencies vs total power

Table 10 RF thruster performance at maximum power (67 W)

Parameter	Value	Parameter	Value
Max Thrust, T_{max}	1.492 mN	Mass utilization efficiency, η_m	90.33%
Max I_{sp}	3168 s	Power efficiency, η_p	49.2%
Max Beam Current, I_{beam}	16.5 mA	Total efficiency, η_{tot}	44.44%

D. Low-thrust trajectory optimization

Earth–Mars transfer trajectory optimization is performed to target a defined ballistic capture point at a set epoch. As the Sun-spacecraft distance increases, the available power decreases and the thruster performance is affected. The spacecraft departs from a distance of 0.01 AU from Earth (Hill sphere radius), outward on the Sun–Earth line. An optimal control problem is solved to minimize a cost function, namely flight time (time-optimal) or propellant consumption (fuel-optimal). Once the spacecraft reaches the capture point, it acquires a highly irregular Mars orbit just by the virtue of natural attractions of Sun and Mars [15]. Optimization involves real solar system dynamics and solar radiation pressure (SRP) [47]. The problem is solved through a direct collocation method to transcribe the optimal control problem to a non-linear programming (NLP) problem. An in-house MATLAB tool called DIRETTO is utilized for transcription of the problem and to supply the NLP solver with the desired inputs [48]. The NLP problem is

solved using the Interior Point OPTimizer - IPOPT tool [49]. Mission start and end epochs are defined and the planet ephemerides are obtained through SPICE Toolkit [50].

The mass of the spacecraft after high-thrust Earth escape is 25.736 kg (see Table 5). The transfer trajectories and the variations of heliocentric eccentricity and semi-major axis for time-optimal and fuel-optimal transfers are illustrated in Figure 9. The time-optimal solution yields a total transfer time of 1200 days (~ 3.28 years), which satisfies EP-01, and the thruster operation time is 1181.8 days. The fuel-optimal solution yields a transfer time of 1350 days (3.83 years).

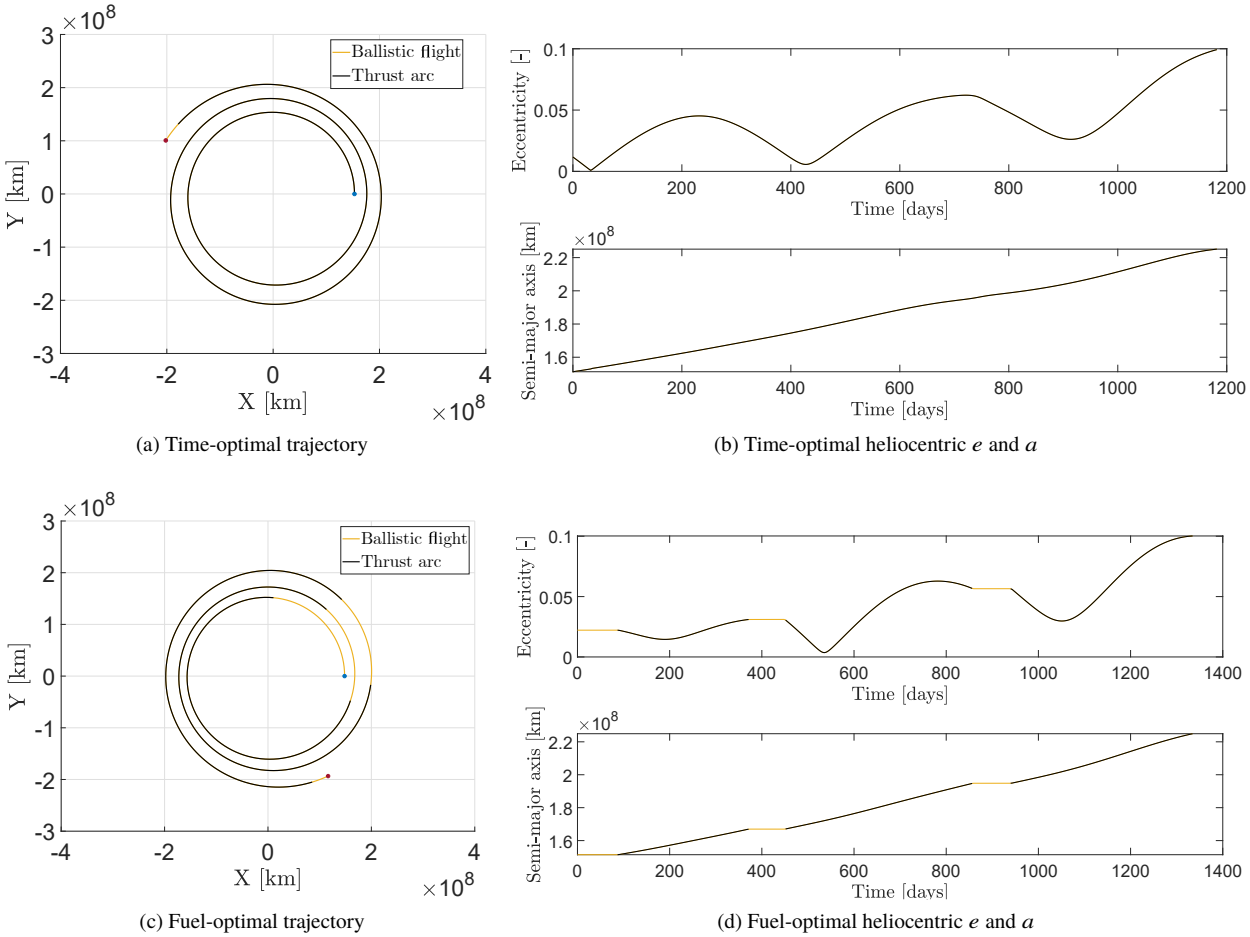

(a) Time-optimal trajectory

(b) Time-optimal heliocentric e and a

(c) Fuel-optimal trajectory

(d) Fuel-optimal heliocentric e and a

Fig. 9 Spacecraft heliocentric trajectory, eccentricity e and semi-major axis a variation in time-optimal and fuel-optimal solutions.

The variations of T and I_{sp} for time-optimal and fuel-optimal transfers are illustrated in Figure 10. The quantities α and β pertain to the azimuthal and elevation thrusting angles, defined in the spacecraft body frame. In the fuel-optimal transfer, the thruster is intermittently switched on and off to save propellant mass. It has to be noted that this bang-bang profile is not imposed apriori but rather found ex-posteriori, thus confirming the appropriateness of the solver. The overall parameters for the time-optimal and fuel-optimal solutions are shown in Table 11.

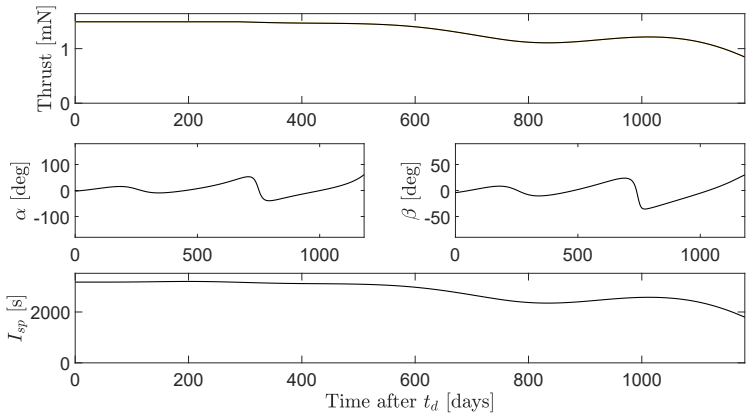

(a) Time-optimal

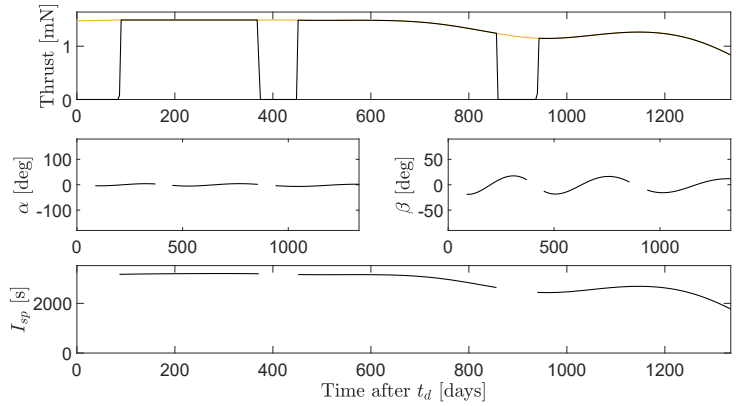

(b) Fuel-optimal

Fig. 10 Thrust and I_{sp} variations over time for time-optimal and fuel-optimal solutions

For the given total transfer time requirements, the mass savings of the fuel-optimal technique is ~0.41 kg for an additional 150 day flight time. The penalty in flight time is considered quite high for the achieved mass saving. Thus, time-optimal transfer is selected.

E. Ballistic capture and circularization

The spacecraft enters a highly irregular orbit about Mars after ballistic capture, which in nature is not closed and some energy needs to be dissipated to close it. The ballistic capture sets are generated using an in-house MATLAB tool, GRATIS [47]. The orbit parameters at the point of capture are $\{a_0, e_0, i_0, \Omega_0, \omega_0, \theta_0\}$ = {434600 km, 0.99, 22.5°, 0°, 326°, 0°}, with the periareion r_{p0} = 4346 km. It is highly inefficient for the scientific observation mission.

The mass of the spacecraft after time-optimal heliocentric transfer is 20.84 kg. Energy dissipation, stabilization, and circularization to a 60000 km orbit are pursued to perform the science mission. The start epoch is set and the chemical propulsion module, with 3 N thurst, provides a retrodirectional ΔV of 45 m/s for stabilization and initial eccentricity reduction. This is done to reduce the overall circularization time since low-thrust propulsion alone would take several

Table 11 Comparison of time-optimal and fuel-optimal heliocentric transfers

	Time-optimal	Fuel-optimal
ΔV	5.792 km/s	5.350 km/s
m_p	4.896 kg	4.488 kg
Total Time	1200 days	1350 days
Thrust time	1181.8 days	1334.48 days

years. The orbit parameters after the chemical burn are $\{a, e, i, \Omega, \omega, \theta\}$ = {86876 km, 0.9499, 22.5°, 360°, 325.8°, 17.88°}. This serves as the initial point for low-thrust circularization.

The strategy to circularize around Mars after the chemical burn involves: a) low-thrust eccentricity reduction and initial circularization, b) low-thrust semi-major axis reduction to desired distance, and c) low-thrust final eccentricity reduction/correction. The thrust and specific impulse of the engine are updated for the corresponding input power at the spacecraft distance from the Sun. The thrust logic is such that the spacecraft is decelerated when closer to Mars (i.e., $r < a$) to reduce the apoapsis and accelerated when farther away from Mars ($r > a$) to increase the periapsis. This is done until the orbit is circularized at a certain semi-major axis. A constant deceleration is then applied to reduce the semi-major axis to 60000 km altitude and finally, the eccentricity is corrected to reach $e = 0.1$ and $r = 63390$ km. The cirularization parameters are listed in Table 12. The circularization completes in 432.23 days while consuming 1.793 kg propellant. Time-optimal heliocentric transfer and circularization using electric propulsion last for 1632.23 days cumulatively.

Table 12 Stabilization and circularization parameters

Parameter	**Value**	**Parameter**	**Value**
Chem-prop ΔV_{stab}	45 m/s	Chem-prop stab. (marg.) $m_{p,stab,mg}$	0.431 kg
Chem-prop burntime	309 s	Elec-prop ΔV	0.867 km/s
Chem-prop (marg.) $\Delta V_{stab,mg}$	49 m/s	Elec-prop Circ. time	432.23 days
Chem-prop stab. $m_{p,stab}$	0.393 kg	Elec-prop Circ. m_p	1.793 kg

The thrust and the specific impulse for the cirularization maneuvers as well as the trajectory are illustrated in Figure 11.

F. System sizing

The time-optimal heliocentric transfer and circularization require an overall propellant mass of 6.69 kg. A ~10% margin is applied on this mass for contingency, which brings it to 7.4 kg. Iodine solid state density is 4940 kg/m^3 and corresponding propellant volume is ~1500 cm^3.

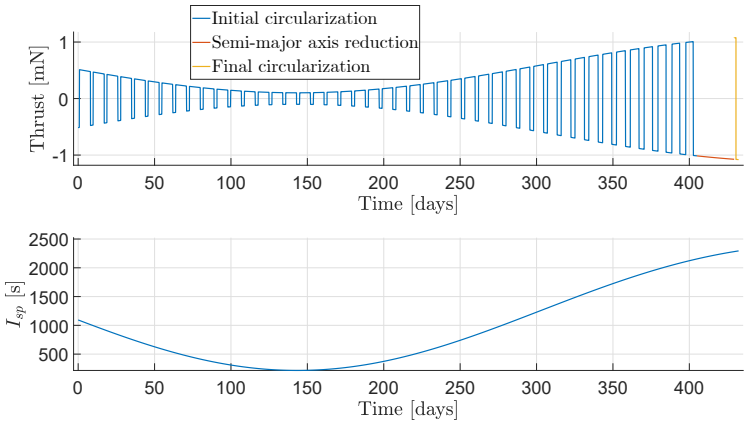

(a) Thrust and I_{sp}

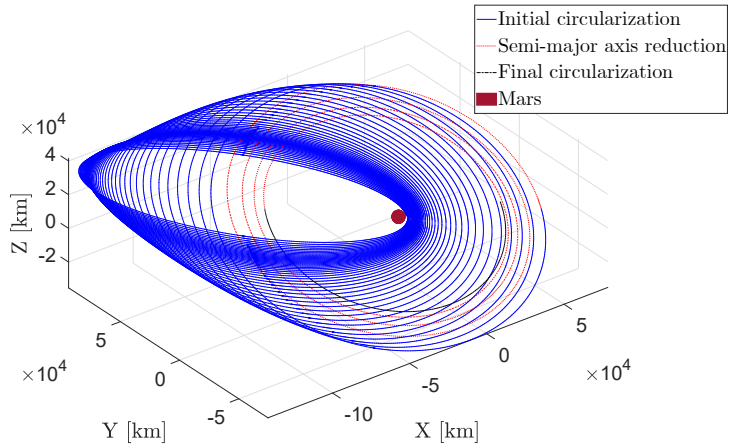

(b) Circularization trajectory

Fig. 11 Thrust and I_{sp} variations, and trajectory during circularization to a 60000 km Mars orbit

The electric propulsion feed system consists of a propellant reservoir where Iodine is stored and sublimated to gas phase (I_2) using a low-power heat source. The resulting vapour is delivered to the thrust chamber using a latch valve and a proportional flow control valve (mass flow control unit) [51]. The vapour pressure of Iodine is 0.3 Torr at 25°C. The flow line must be heated to keep the Iodine in the vapour state, although it requires <1W power to maintain a 10 mg/s flow of I_2 [52]. Owing to the low storage pressure, the reservoir tank is thin walled and made of a thermoplastic material [39].

The propellant tank is sized to contain solid Iodine and the low-power heat source. The latter occupies 5% of the volume. Additionally, a 5% ullage volume is allocated for the sublimated gas. A tank volume of 1650 cm^3 is utilized and the dimensions are 20 cm × 10 cm × 8.25 cm, which is ~1.7U. The tank mass amounts to 0.02 kg. Inclusion of the feed lines, valves, and PPCU volumes brings the total volume to 3U. The electric propulsion system schematic is illustrated in Figure 12. The overall design parameters of the electrical propulsion system are summarized in Table 13.

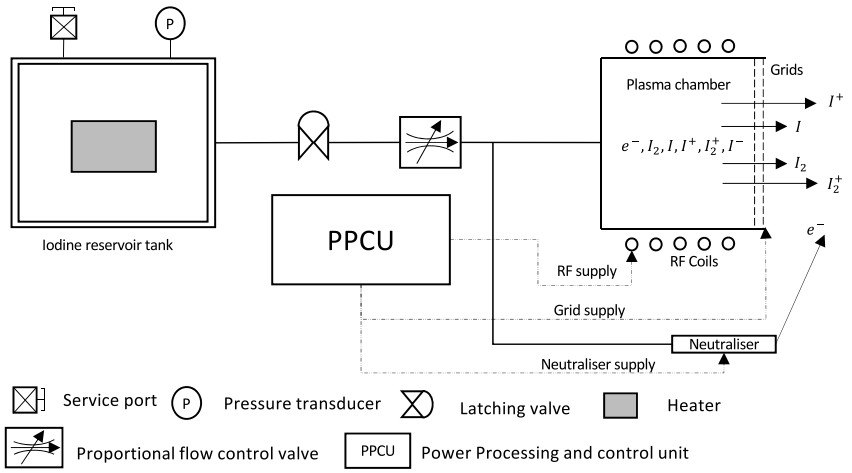

Fig. 12 Schematic of the electric propulsion system

Table 13 Electric propulsion design parameters

Parameter	Value	Parameter	Value
Propellant mass, $m_{p,mg}$	7.4 kg	Feed sys. mass, m_{feed}	0.5 kg
PPCU Mass, m_{PPCU}	0.2 kg	Thruster mass, m_T	0.2 kg
Tank volume	1650 cm^3	Tank dimension	20× 10×8.25 cm^3
EP total mass, $m_{ep,sys}$	8.3 kg	EP total volume, $V_{ep,sys}$	3U

V. Discussion and conclusion

The concept of combined chemical–electric propulsion on-board CubeSats enables scientifically significant, operations-wise timely, and cost-efficient Solar System exploration missions. Traditionally, interplanetary missions have either used fully chemical or fully electric propulsion systems. The former leads to a very large propellant mass, which is unaffordable for a CubeSat, and a very short transfer time. The latter leads to a very long transfer time and high radiation damage due to multiple crossings of the Van Allen belts but yields a very low propellant mass. The idea behind this work was to provide a significantly detailed characterization of propulsion solutions using which stand-alone CubeSat missions to Mars can be achieved while balancing time and system mass.

The proposed solution for chemical stage comprises an advanced high performance green monopropellant system utilizing FLP-106 propellant to execute Earth escape. Thruster performance analysis yields 3.072 N thrust and 241.2 s specific impulse. A high-thrust trajectory simulation with multiple orbit raising maneuvers is performed and the system design parameters are delineated. The electric propulsion stage comprises an Iodine-propelled miniature RF ion thruster to execute a deep-space Earth–Mars transfer. A comprehensive global thruster performance model is implemented and the dependence of thrust and I_{sp} on input power are obtained, with maximum values being 1.49 mN and 3168 s, respectively. An optimal control problem is solved for low-thrust trajectory optimization of the Earth–Mars transfer

utilizing the calculated RF thruster performances. For the 30 kg 16U CubeSat mission, the chemical and electric propulsion systems weigh ~6.59 kg (21.96%) and 8.3 kg (27.66%), respectively. The volumes occupied are 7.5U (chemical) and 3U (electric). The transfer time from SSGTO to a 60000 km Mars circular orbit is ~1650 days or 4.52 years. The solution is feasible with respect to time and system constraints.

Multiple points of improvement shall be addressed in the further stages of this research. Firstly, chemical propulsion system design could be further refined by performing in-depth CFD analyses and experiments to determine the full-scale system performances. A combined analysis of chemical propulsion and attitude control system is required for optimizing operations. Although there are reaction wheels and reaction control systems that can handle a ~3 N thrust on small spacecraft, a detailed analysis would be useful for fine-tuning the throttle control. Electric propulsion systems utilizing Iodine propellant are at their nascent stage of development. A higher level of system maturation and space qualification is yet to be achieved.

Currently, the authors are pursuing a research on the development of a combined propulsion systems–hybrid trajectory design framework. The low-thrust trajectory and electric propulsion system performance are simultaneously optimized to provide a global solution for the heliocentric transfer. Combined high-thrust trajectory and chemical propulsion performance optimization yields effective maneuver spreading and minimization of radiation damage. These analyses will lead to *sensible* design of the mission and the spacecraft.

Enabling combined chemical–electric propulsion system shall lead to a major paradigm shift in solar system exploration efforts using CubeSats at a very high science-to-investment ratio. Although the risk is higher than that of traditional interplanetary missions, the gain is significantly high.

Acknowledgment

This work was pursued as a collaborative effort between Politecnico di Milano, Italy and Delft University of Technology, the Netherlands. Special thanks to PhD School of Politecnico di Milano for providing IDEA League Students Research Grant. The authors would like to thank Mr. Stefano Boccelli, Mr. Gonçalo Cruz Chambel de Aguiar, Mr. Álvaro Sanz Casado and Mr. Fernando Soler Lanagrán for their useful and timely contributions.

References

[1] Zurbuchen, T. H., von Steiger, R., Bartalev, S., Dong, X., Falanga, M., Fléron, R., Gregorio, A., Horbury, T. S., Klumpar, D., Küppers, M., et al., "Performing High-Quality Science on CubeSats," *Space Research Today*, Vol. 196, Jan 2016, pp. 11–30. doi:10.1016/j.srt.2016.07.011.

[2] Conversano, R. W., and Wirz, R. E., "Mission capability assessment of CubeSats using a miniature ion thruster," *J.Spacecraft Rockets*, Vol. 50, No. 5, 2013, pp. 1035–1046. doi:10.2514/1.A32435.

[3] Spangelo, S., and Longmier, B., "Optimization of CubeSat System-Level Design and Propulsion Systems for Earth-Escape Missions," *Journal of Spacecraft and Rockets*, Vol. 52, No. 4, 2015, pp. 1009–1020. doi:10.2514/1.A33136.

[4] Hudson, J., Spangelo, S., Hine, A., Kolosa, D., and Lemmer, K., "Mission analysis for Cubesats with micropropulsion," *Journal of Spacecraft and Rockets*, Vol. 53, No. 5, 2016, pp. 836–846. doi:10.2514/1.A33564.

[5] Poghosyan, A., and Golkar, A., "CubeSat evolution: Analyzing CubeSat capabilities for conducting science missions," *Progress in Aerospace Sciences*, Vol. 88, Jan 2017, pp. 59–83. doi:10.1016/j.paerosci.2016.11.002.

[6] Mueller, J., Hofer, R., and Ziemer, J., "Survey of Propulsion Technologies Applicable to Cubesats," *Joint Army Navy NASA Air Force (JANNAF) Propulsion Meeting, Colorado Springs, United States*, May 2010, p. 1646.

[7] Lemmer, K., "Propulsion for CubeSats," *Acta Astronautica*, Vol. 134, May 2017, pp. 231–243. doi:10.1016/j.actaastro.2017.01.048.

[8] Rayburn, C. D., Campbell, M. E., and Mattick, A. T., "Pulsed plasma thruster system for microsatellites," *Journal of Spacecraft and Rockets*, Vol. 42, No. 1, 2005, pp. 161–170. doi:10.2514/1.15422.

[9] Charles, C., Boswell, R., Alexander, P., Costa, C., Sutherland, O., Pfitzner, L., Franzen, R., Kingwell, J., Parfitt, A., Frigot, P.-E., et al., "Helicon double layer thrusters," *42nd AIAA - American Society of Mechanical Engineers - Society of Automotive Engineers - American Society for Engineering Education Joint Propulsion Conference & Exhibit*, July 2006, p. 4838.

[10] Berg, S. P., and Rovey, J. L., "Assessment of multimode spacecraft micropropulsion systems," *Journal of Spacecraft and Rockets*, Vol. 54, No. 3, 2017, pp. 592–601. doi:10.2514/1.A33649.

[11] Staehle, R., Blaney, D., Hemmati, H., Lo, M., Mouroulis, P., Pingree, P., Wilson, T., Puig-Suari, J., Williams, A., Betts, B., et al., "Interplanetary CubeSats: opening the solar system to a broad community at lower cost," *Journal of Small Satellites*, Vol. 2, No. 1, 2013, pp. 161–186.

[12] Klesh, A., Clement, B., Colley, C., Essmiller, J., Forgette, D., Krajewski, J., Marinan, A., Martin-Mur, T., Steinkraus, J., Sternberg, D., et al., "MarCO: Early Operations of the First CubeSats to Mars," *32nd Annual AIAA/USU Conference on Small Satellites, Logan, Utah, United States*, Aug 2018, pp. 1–10.

[13] Walker, R., Binns, D., Bramanti, C., Casasco, M., Concari, P., Izzo, D., Feili, D., Fernandez, P., Fernandez, J. G., Hager, P., et al., "Deep-space CubeSats: thinking inside the box," *Astronomy and Geophysics*, Vol. 59, No. 5, 2018, pp. 5–24. doi:10.1093/astrogeo/aty232.

[14] Wood, J. A., Boynton, W. V., Buck, W. R., Ferris, J. P., Hayes, J. M., Meech, K. J., Mustard, J. F., Nagy, A. F., Noll, K. S., Paige, D. A., Pappalardo, R. T., Reysenbach, A.-L., Schopf, J. W., and Sprague, A. L., *Assessment of Mars science and mission priorities*, Space Studies Board, National Research Council, National Academies Press, Washington D.C, 2003. ISBN: 978-0309089173.

[15] Topputo, F., and Belbruno, E., "Earth–Mars transfers with ballistic capture," *Celestial Mechanics and Dynamical Astronomy*, Vol. 121, No. 4, 2015, pp. 329–346. doi:10.1007/s10569-015-9605-8.

[16] ESA-ESTEC, "CDF Study Report of Lunar Meteoroid Impacts Observer (LUMIO) Mission," Tech. Rep. LUMIO-CDF-R-36, European Space Agency, Noordwijk, the Netherlands, May 2018.

[17] Hegel, D., "Flexcore: Low-cost attitude determination and control enabling high-performance small spacecraft," *30th Annual AIAA/USU Conference on Small Satellites, Logan, Utah, United States*, Aug 2016, pp. 1–8.

[18] Gohardani, A. S., Stanojev, J., Demairé, A., Anflo, K., Persson, M., Wingborg, N., and Nilsson, C., "Green space propulsion: Opportunities and prospects," *Progress in Aerospace Sciences*, Vol. 71, Nov 2014, pp. 128–149. doi:10.1016/j.paerosci.2014.08.001.

[19] Scharlemann, C., and Tajmar, M., "Development of Propulsion Means for Microsatellites," *43rd AIAA - American Society of Mechanical Engineers - Society of Automotive Engineers - American Society for Engineering Education Joint Propulsion Conference & Exhibit*, July 2007, p. 5184.

[20] Anflo, K., and Crowe, B., "In-space demonstration of an ADN-based propulsion system," *47th AIAA - American Society of Mechanical Engineers - Society of Automotive Engineers - American Society for Engineering Education Joint Propulsion Conference & Exhibit*, July 2011, p. 5832.

[21] Wurdak, M., Strauss, F., Werling, L., Ciezki, H. K., Greuel, D., Lechler, R., Wingborg, N., Hasan, D., and Scharlemann, C., "Determination of fluid properties of the green propellant FLP-106 and related material and component testing with regard to applications in space missions," *3rd Space Propulsion Conference, Bordeaux, France*, 3AF - Association Aéronautique et Astronautique de France, May 2012, pp. 1–8.

[22] Negri, M., "Replacement of hydrazine: overview and first results of the H2020 project Rheform," *6th European Conference for Aeronautics and Space Sciences (EUCASS), Krakow, Poland*, June 2015, pp. 29–06.

[23] Gordon, S., and McBride, B. J., "Computer program for calculation of complex chemical equilibrium compositions and applications. Part 1: Analysis," Tech. Rep. NASA-RP-1311, National Aeronautics and Space Administration. Glenn Research Center, Cleveland, Oct 1994.

[24] Vatani, A., Mehrpooya, M., and Gharagheizi, F., "Prediction of Standard Enthalpy of Formation by a QSPR Model," *International Journal of Molecular Sciences*, Vol. 8, No. 5, 2007, pp. 407–432. doi:10.3390/i8050407.

[25] Kon'kova, T. S., Matyushin, Y. N., Miroshnichenko, E. A., and Vorob'ev, A. B., "Thermochemical properties of dinitramidic acid salts," *Russian Chemical Bulletin*, Vol. 58, No. 10, 2009, pp. 2020–2027. doi:10.1007/s11172-009-0276-z.

[26] Rumble, J., *CRC Handbook of Chemistry and Physics*, 99$^{\text{th}}$ ed., CRC Press, Boca Raton, Florida, 2018. ISBN: 978-1439880494.

[27] Spores, R. A., "GPIM AF-M315E Propulsion System," *51st AIAA - Society of Automotive Engineers - American Society for Engineering Education Joint Propulsion Conference*, American Institute of Aeronautics and Astronautics, July 2015, p. 3573.

[28] Negri, M., Wilhelm, M., Hendrich, C., Wingborg, N., Gediminas, L., Adelöw, L., Maleix, C., Chabernaud, P., Brahmi, R., Beauchet, R., et al., "New technologies for ammonium dinitramide based monopropellant thrusters–The project RHEFORM," *Acta Astronautica*, Vol. 143, Feb 2018, pp. 105–117. doi:10.1016/j.actaastro.2017.11.016.

[29] Werling, L. K., Haßler, M., Lauck, F., Ciezki, H. K., and Schlechtriem, S., "Experimental Performance Analysis (c* & c* Efficiency) of a Premixed Green Propellant consisting of N2O and C2H4," *53rd AIAA - Society of Automotive Engineers - American Society for Engineering Education Joint Propulsion Conference*, July 2017, p. 5069.

[30] Wilhelm, M., Negri, M., Ciezki, H., and Schlechtriem, S., "Preliminary tests on thermal ignition of ADN-based liquid monopropellants," *Acta Astronautica*, Vol. 158, May 2018, pp. 388–396. doi:10.1016/j.actaastro.2018.05.057.

[31] Wingborg, N., Larsson, A., Elfsberg, M., and Appelgren, P., "Characterization and ignition of ADN-based liquid monopropellants," *41st AIAA - American Society of Mechanical Engineers - Society of Automotive Engineers - American Society for Engineering Education Joint Propulsion Conference & Exhibit*, July 2005, p. 4468.

[32] Sutton, G. P., and Biblarz, O., *Rocket propulsion elements*, 7th ed., John Wiley & Sons, New York, 2010, Chaps. 3, 9, pp. 55–68 & 90–92 & 282–284 & 342. ISBN: 978-0471326427.

[33] Jens, E., Karp, A. C., Nakazono, B., Eldred, D. B., DeVost, M. E., and Vaughan, D., "Design of a Hybrid CubeSat Orbit Insertion Motor," *52nd AIAA - Society of Automotive Engineers - American Society for Engineering Education Joint Propulsion Conference*, July 2016, p. 4961.

[34] *RNH 64-1 Technical Data Sheet*, Eagle Picher Technologies, Feb 2003. URL `https://www.datasheetarchive.com/companies/eaglepicher_com.html`, Last Accessed: 30-March-2019.

[35] Wertz, J. R., Everett, D. F., and Puschell, J. J., *Space mission engineering: the new SMAD*, Microcosm Press, Hawthorne, California, 2011, Chap. 18, pp. 545–546. ISBN: 978-1881883159.

[36] Welsch, G., Boyer, R., and Collings, E., *Materials properties handbook: titanium alloys*, ASM international, 1993. ISBN: 978-0871704818.

[37] Huzel, D. K., *Modern engineering for design of liquid-propellant rocket engines*, AIAA, 1992, Vol. 147, Chap. 8, pp. 289–304. ISBN: 978-1563470134.

[38] Sato, E., Sawai, S., Uesugi, K., Takami, T., Furukawa, K., Kamada, M., and Kondo, M., "Superplastic Titanium Tanks for Propulsion System of Satellites," *Materials Science Forum*, Vol. 551-552, July 2007, pp. 43–48. doi:10.4028/www.scientific.net/msf.551-552.43.

[39] Tsay, M., Frongillo, J., and Zwahlen, J., "Maturation of iodine fueled BIT-3 RF ion thruster and RF neutralizer," *52nd AIAA - Society of Automotive Engineers - American Society for Engineering Education Joint Propulsion Conference*, July 2016, p. 4544.

[40] Mazouffre, S., "Electric propulsion for satellites and spacecraft: established technologies and novel approaches," *Plasma Sources Science and Technology*, Vol. 25, No. 3, 2016, p. 033002. doi:10.1088/0963-0252/25/3/033002.

[41] Tsay, M., Frongillo III, J. J., Model, J., and Zwahlen, J., "Iodine propellant rf ion thruster with rf cathode," , 2018. US Patent App. 15/425,317.

[42] Branam, R. D., "Iodine Plasma (Electric Propulsion) Interaction with Spacecraft Materials," Tech. Rep. AFRL-AFOSR-VA-TR-2016-0381, The University of Alabama Tuscaloosa & Air Force Research Laboratory, United States, Dec 2016.

[43] Polzin, K. A., Peeples, S. R., Seixal, J. F., Mauro, S. L., Lewis, B. L., Jerman, G. A., Calvert, D. H., Dankanich, J., Kamhawi, H., Hickman, T. A., et al., "Propulsion system development for the iodine satellite (iSAT) demonstration mission," *Joint Conference 30th International Symposium on Space Technology and Science, 34th International Electric Propulsion Conference and 6th Nanosatellite Symposium, Kobe, Japan*, July 2015, pp. 1–14.

[44] Grondein, P., Lafleur, T., Chabert, P., and Aanesland, A., "Global model of an iodine gridded plasma thruster," *Physics of Plasmas*, Vol. 23, No. 3, 2016, p. 033514. doi:10.1063/1.4944882.

[45] Goebel, D. M., and Katz, I., *Fundamentals of electric propulsion: ion and Hall thrusters*, John Wiley & Sons, New York, 2008, Vol. 1, Chaps. 4,6, pp. 148,251–255. ISBN: 978-0470436448.

[46] Chabert, P., Arancibia Monreal, J., Bredin, J., Popelier, L., and Aanesland, A., "Global model of a gridded-ion thruster powered by a radiofrequency inductive coil," *Physics of Plasmas*, Vol. 19, No. 7, 2012, p. 073512. doi:10.1063/1.4737114.

[47] Aguiar, G., and Topputo, F., "A technique for designing Earth–Mars low-thrust transfers culminating in ballistic capture," *7th International Conference on Astrodynamics Tools and Techniques (ICATT)*, Oberpfaffenhofen, Germany, Nov 2018, pp. 1–8.

[48] Topputo, F., and Zhang, C., "Survey of Direct Transcription for Low-Thrust Space Trajectory Optimization with Applications," *Abstract and Applied Analysis*, Vol. 1, June 2014, pp. 1–15. doi:10.1155/2014/851720.

[49] Byrd, R. H., Hribar, M. E., and Nocedal, J., "An interior point algorithm for large-scale nonlinear programming," *Society for Industrial and Applied Mathematics (SIAM) Journal on Optimization.*, Vol. 9, No. 4, 1999, pp. 877–900. doi:10.1137/s1052623497325107.

[50] Acton Jr, C. H., "Ancillary data services of NASA's navigation and ancillary information facility," *Planetary and Space Science*, Vol. 44, No. 1, 1996, pp. 65–70. doi:10.1016/0032-0633(95)00107-7.

[51] Holste, K., Gärtner, W., Zschätzsch, D., Scharmann, S., Köhler, P., Dietz, P., and Klar, P. J., "Performance of an iodine-fueled radio-frequency ion-thruster," *European Physical Journal D*, Vol. 72, No. 1, 2018, p. 9. doi:10.1140/epjd/e2017-80498-5.

[52] Dressler, R., Chiu, Y.-H., and Levandier, D., "Propellant alternatives for ion and Hall effect thrusters," *38th AIAA Aerospace Sciences Meeting and Exhibit*, Jan 2000, p. 602.